Selectivity control between reverse water-gas shift and fischer-tropsch synthesis in carbon-supported iron-based catalysts for CO_2 hydrogenation

Meng, Weixin; de Jong, Bart C.A.; van de Bovenkamp, Henk V.; Boer, Gert Jan; Leendert Bezemer, G.; Iulian Dugulan, A.; Xie, Jingxiu

DOI
10.1016/j.cej.2024.151166

Publication date
2024

Document Version
Final published version

Published in
Chemical Engineering Journal

Chemical Engineering Journal 489 (2024) 151166

Contents lists available at ScienceDirect

Chemical Engineering Journal

journal homepage: www.elsevier.com/locate/cej

Selectivity control between reverse water-gas shift and fischer-tropsch synthesis in carbon-supported iron-based catalysts for CO_2 hydrogenation

Weixin Meng [a,1], Bart C.A. de Jong [a,1], Henk van de Bovenkamp [a], Gert-Jan Boer [a], G. Leendert Bezemer [b], A. Iulian Dugulan [c], Jingxiu Xie [a,*]

[a] Green Chemical Reaction Engineering, Engineering and Technology Institute Groningen, University of Groningen, Nijenborgh 4 9747 AG Groningen, the Netherlands
[b] Energy Transition Campus Amsterdam, Shell Global Solutions International B.V., Grasweg 31, 1031 HW Amsterdam, the Netherlands
[c] Laboratory of Fundamentals Aspects of Materials and Energy, Department of Radiation Science & Technology, Delft University of Technology, Mekelweg 15, 2628 CD Delft, the Netherlands

ARTICLE INFO

Keywords:
Fe-based catalysts
Particle size
CO_2 hydrogenation
RWGS
FTS

ABSTRACT

CO_2 hydrogenation to chemicals and fuels has the potential to alleviate CO_2 emissions and displace fossil resources simultaneously via consecutive RWGS and FTS reactions, also known as CO_2-FTS. As Fe-based catalysts are active and selective for both reactions, their bifunctionality requires a delicate balance between the RWGS and FTS. In this work, we investigated the thermodynamic constraints of RWGS and CO_2-FTS, the influence of CO_2 conversion on selectivity and the influence of Fe nanoparticle size within the range of 4.7 to 10.3 nm. An inert carbon support was selected to rule out metal-support interaction and promoting effects of the support. Catalytic performance was evaluated at 300 °C, 11 bar, $H_2/CO_2/Ar = 3/1/1$, 600 to 72000 $mL \cdot g_{cat}^{-1} \cdot h^{-1}$. At a CO_2 conversion level below RWGS equilibrium conversion of 23 %, RWGS was found to be the primary and dominant reaction. No primary Sabatier reaction was observed. At higher CO_2 conversion till the CO_2-FTS threshold of 42 %, the secondary FTS reaction became dominant. Notably, a non-linear relation between CO_2 conversion and CO selectivity was discovered. Comparing two catalysts with identical 5 wt% Fe loading but different average Fe nanoparticle size (6.6 and 8.4 nm), the 8.4 nm Fe catalyst was at least two times more active than the 6.6 nm Fe catalyst. In situ Mössbauer spectroscopy suggested a positive correlation between particle size, carburization and selectivity towards long-chain hydrocarbons. For these potassium-promoted carbon-supported Fe-based catalysts, nanoparticles of at least 8 nm are required for the formation of Fe carbides and improved reactivity.

1. Introduction

The valorization of CO_2 into value-added chemicals and fuels is a viable solution to mitigate carbon dioxide emissions and fossil fuel consumption, thereby contributing to a circular carbon economy [1–3]. A strategy of CO_2 hydrogenation to long-chain hydrocarbons (CO_2-FTS) is to reduce CO_2 to CO via the reverse water gas shift (RWGS) reaction prior to the conversion of CO to hydrocarbons via Fischer-Tropsch synthesis (FTS) [4–6]. The endothermic RWGS reaction is favorable at temperatures higher than 500 °C, while the exothermic FTS reaction operates at lower temperatures between 200 and 350 °C [7–9]. At 300 °C and $H_2/CO_2 = 3$, the RWGS equilibrium CO_2 conversion is 23 %. In addition, the selectivity of long-chain hydrocarbons has an inverse relationship with temperature [10]. As FTS is a surface polymerization reaction, the hydrocarbon distribution is governed by the Anderson-Schulz-Flory (ASF) model [11].

Among the FTS elements (Fe, Co, Ni, Ru, and Rh), Fe-based catalysts are promising candidates due to their ability to catalyze both RWGS and FTS reactions via the active phases of Fe_3O_4 and Fe_5C_2 respectively [12–14]. When these Fe phases are dispersed on supports, mechanical stability and nanoparticle dispersion are improved in comparison to its bulk Fe-based counterparts [15,16]. Hydrocarbon product selectivity is dependent on many factors including morphology and particle size of metal nanoparticles, supports, promoters, and reaction conditions [17–22]. Inert supports such as carbon are advantageous as the formation of irreducible Fe species with the support such as Fe aluminate can be avoided [23,24]. To increase the hydrocarbon chain growth probability (α), Fe-based catalysts are often promoted with alkali metals and

* Corresponding author.
E-mail address: jingxiu.xie@rug.nl (J. Xie).
[1] Both authors contributed equally to this work.

https://doi.org/10.1016/j.cej.2024.151166

Available online 9 April 2024

transition metals [25–28]. Potassium (K) is one of the most effective promoters for Fe-based catalysts since it is an electronic promoter for both RWGS and FTS [29–31].

The nanoparticle size plays an important role in the catalytic performance due to the structure sensitivity of both RWGS and FTS [15,32–34]. The particle size predominantly controls the exposed active sites on different surface regions, such as edge, corner, terrace, and step, exhibiting distinguishable catalytic properties due to their unique coordination and bonding [35]. Zhu et al. studied the particle size effects of Fe/ZrO_2 catalysts at 320 °C, 30 bar, $H_2/CO_2 = 3$, 18000 mL·g_{cat}^{-1}·h^{-1}. Catalysts with 15 wt% Fe loading and average Fe particle sizes from 3 to 13 nm were attained by varying the zirconia support surface area. The primary reactions, RWGS and Sabatier, were found to be more structure sensitive in the particle size range of 6 to 13 nm. On the other hand, the secondary FTS reaction was more sensitive within the range of 3 to 10 nm [36]. Song et al. used the pore sizes of an alumina support to prepare catalysts with 10 wt% Fe loading and average Fe particle sizes between 5 and 23 nm. At 400 °C, 30 bar, $H_2/CO_2 = 3$, 3600 mL·g_{cat}^{-1}·h^{-1}, average Fe_2O_3 particle sizes of 5 to 8 nm were reported to be the most active for CO_2 hydrogenation to hydrocarbons [37]. These prior studies indicate that CO_2-FTS is indeed a structure-sensitive process, and shed insights into the impact of the Fe nanoparticle size. However, these studies were performed with Fe nanoparticles dispersed on oxidic supports which were either reactive for the reactants or prone to have the drawback of potential formation of irreducible species like iron aluminate during preparation, reduction or catalytic testing.

In this study, the aim is to investigate the influences of Fe nanoparticle size and dispersion on the interplay between RWGS and FTS in the CO_2-FTS process. An inert carbon support was selected to rule out metal-support interactions and promoting effects of the support. The carbon-supported Fe-based catalysts with K promoter were prepared via incipient wetness impregnation. By varying the Fe loading from 2 wt% to 20 wt%, as well as temperature and duration of calcination, catalysts containing Fe oxide nanoparticles with the average particle size range of 4 to 10 nm were obtained. Taking thermodynamic considerations into account, the effects of Fe nanoparticle size and dispersion on the reactivity of RWGS and FTS were elucidated at 300 °C, 11 bar, $H_2/CO_2/Ar$ = 3/1/1, 600-72000 mL·g_{cat}^{-1}·h^{-1}. In-situ Mössbauer spectroscopy was used to identify the evolution of the Fe phase under reduction, carburization, and reaction conditions.

2. Experimental methods

2.1. Catalyst preparation

The carbon-supported Fe-based catalysts with 2, 5, 10, and 20 wt% Fe weight loading (with K promoter) were prepared by incipient wetness impregnation. Ammonium iron citrate (Sigma-Aldrich, 16.5-18.5 wt% Fe) and potassium nitrate (Sigma-Aldrich, ≥ 99.0 %) were first dissolved in deionized water. For 1 g of salt precursor, 1 mL of deionized water was used. Methanol was subsequently added to aqueous precursor solution, and 0.5 mL of methanol was used for 1 mL of deionized water. The Fe/K molar ratio was fixed at 10 for all catalysts. The solution was added dropwise to the carbon black support (Cabot, VXC 72, 100 %, 75-150 μm) and the sample was dried in the oven at 120 °C overnight. For 2 and 5 wt% Fe-K/C samples, diluted solutions were required to fill the pore volume of the carbon support. For the 20 wt% Fe-K/C sample, successive impregnation steps were required, and the batches were dried in the oven at 120 °C for 1 h between each step. After drying, the samples were pyrolyzed at 500 °C (2 °C/min) for 2 h under N_2 flow. In order to get a larger average Fe particle size, the 5 wt% Fe-K/C catalyst was pyrolyzed at 700 °C for 8 h and the 20 wt% Fe-K/C catalyst was pyrolyzed at 500 °C for 32 h under N_2 flow. The catalysts were referred to according to the average Fe oxide particle size in the fresh catalysts from TEM analysis, e.g. 7.7 nm Fe showed an average Fe oxide particle size of 7.7 nm.

2.2. Characterization

Inductively Coupled Plasma-Optical Emission Spectrometry (ICP-OES) was used to determine the elemental loading of Fe and K. Additional elemental analysis using X-ray fluorescence (XRF) was performed with a PerkinElmer Optima 7000 DV with a solid-state CCD array detector. Transmission electron microscopy (TEM) was employed to determine the average Fe nanoparticle size and distribution on the carbon support. TEM measurements were conducted on a Philips CM120 microscope operated at an acceleration voltage of 120 kV. The sample was ultrasonically suspended in ethanol and dispersed over a carbon-coated Cu grid. At least 200 Fe nanoparticles were measured to attain the number averaged particle size. N_2 physisorption was carried out with a Micromeritics ASAP 2420 analyzer. The specific surface area was calculated using the Brunauer-Emmett-Teller (BET) method. The pore volume was obtained from the single point desorption data at P/ P ° = 0.98. The pore size was measured using the Barrett-Joyner-Halenda (BJH) method with the desorption branch. Before the analysis, the samples were degassed at 200 °C for 12 h. X-ray diffraction (XRD) was applied to identify Fe crystal structure and phase. The XRD pattern was recorded on a Bruker D8 Advance diffractometer at 40 kV and 40 mA using Cu-Kα radiation (λ = 1.5544 Å). The data was collected under the 2θ of 20° to 90° with a step size of 0.02 and a scan time of 0.75 s.

In-situ transmission Fe Mössbauer spectroscopy was used to determine the composition of Fe phases in fresh, reduced, carburized and CO_2-FTS samples. Transmission ^{57}Fe Mössbauer spectra were collected at 120 K with a sinusoidal velocity spectrometer using a ^{57}Co(Rh) source. Velocity calibration was carried out using an α-Fe foil at room temperature. The source and the absorbing samples were kept at the same temperature during the measurements. The Mössbauer spectra were fitted using the Mosswinn 4.0 program. The experiments were performed in a state-of-the-art high-pressure Mössbauer in-situ cell - developed at Reactor Institute Delft. The high-pressure beryllium windows used in this cell contain 0.08 % Fe impurity whose spectral contribution was fitted and removed from the final spectra. The conditions were the same as for the catalytic experiments, which are described below.

2.3. Catalyst performance

The catalytic experiments were performed in a fixed-bed reactor setup (Microactivity Effi, PID Eng) containing 0.1-1 g of catalyst (75-150 μm) diluted with SiC (25-75 μm). Prior to the reaction, the catalysts were reduced with diluted H_2 ($H_2/Ar = 1/1$) flow at 400 °C (5 °C/min) for 2 h, followed by H_2/CO ($H_2/CO/Ar = 2/2/1$) carburization at 280 °C for 20 h. After reduction and carburization, the catalysts were evaluated at 300 °C, 11 bar, $H_2/CO_2/Ar$ = 3/1/1, 600-72000 mL·g_{cat}^{-1}·h^{-1}. The products were analyzed online with a GC equipped with three channels and detectors. A channel with a thermal conductivity detector was used for permanent gases, and two channels with flame ionization detectors were used for paraffins/olefins and oxygenates.

The CO_2 conversion and the product selectivity were calculated according to equations (1) and (2). The CO-free hydrocarbon selectivity was calculated considering only hydrocarbon production in the CO_2 hydrogenation (equation (3)). The carbon balance was between 85-104 %, excluding less than 1 % selectivity towards oxygenates.

$$X_{CO_2} = \frac{CO_{2,in} - \frac{Ar_{in}}{Ar_{out}} * CO_{2,out}}{CO_{2,in}} * 100\% \quad (1)$$

$$S_{product} = \frac{\frac{Ar_{in}}{Ar_{out}} * product_{out} * n}{CO_{2,in} - \frac{Ar_{in}}{Ar_{out}} * CO_{2,out}} * 100\% \quad (2)$$

$$S_{C_nH_m} = \frac{\frac{Ar_{in}}{Ar_{out}} * n * C_nH_{mout}}{\sum(\frac{Ar_{in}}{Ar_{out}} * n * C_nH_{mout})} * 100\% \quad (3)$$

Where $CO_{2,in}$ and $CO_{2,out}$ represent the molar concentration of CO_2 in the feed and product stream respectively; Ar_{in} and Ar_{out} represent the molar concentration of Ar in the feed and product stream respectively; $product_{out}$ and $C_nH_{m\,out}$ represent the molar concentration of products and n presents the number of carbon atoms in the product.

3. Result and discussion

3.1. Chemical and physical properties of catalysts

The properties of fresh carbon-supported Fe-based catalysts are presented in Table 1. By varying the Fe loading (2 to 20 wt%), as well as the temperature and duration of pyrolysis, catalysts containing Fe oxide nanoparticles with an average particle size ranging between 4.7 and 10.3 nm were obtained. The increase in Fe loading correlated with the decrease in surface area and pore volume of the carbon support. From Fig. 1, the XRD patterns exhibited peaks at 2θ = 30.2°, 35.6°, 43.3°, 57.3 °and 62.9°, corresponding to γ-Fe_2O_3 (220), (311), (400), (511) and (440) respectively (JCPDS 39-1346) [38]. No obvious peaks could be observed for the 4.7 nm Fe due to the small crystallite size of Fe_2O_3. The peak at 2θ = 26° corresponded to the carbon support, and the lack of peaks for potassium oxide indicated the absence of crystalline potassium nanoparticles so a high dispersion of potassium is achieved.

Fig. 2 shows the TEM images of fresh catalysts, verifying the Fe particles supported on the carbon. All catalysts exemplified a homogenous Fe dispersion even at high Fe loadings due to the synthesis strategy. First, the addition of methanol to the aqueous precursor solution ensured a good wettability and contact between the precursor solution and the unfunctionalized hydrophobic carbon support. Second, the utilization of the citrate precursor prevented the aggregation of Fe nanoparticles during calcination, leading to a narrow Fe particle size distribution (Fig. S1). As a comparison, a catalyst prepared with Fe nitrate as precursor displayed a worse Fe dispersion, larger average particle size of 20.1 nm and broad size distribution (Fig. S2).

3.2. CO_2 conversion constraints and pathway of CO_2-FTS

Fig. 3(a) shows CO_2 conversion as a function of residence time in the reactor. A positive relation between CO_2 conversion and residence time was expected and could be observed, except when CO_2 conversion was approaching the RWGS equilibrium conversion and CO_2-FTS conversion threshold. The thermodynamic equilibrium conversion of RWGS at 300 °C, 11 bar, H_2/CO_2 = 3 is 23 %, and the consumption of CO by the FTS reaction allows equilibrium conversion to be shifted up to 42 %. The threshold of CO_2 conversion at 42 % is attributed to the thermodynamic constraints from a decreased CO partial pressure and kinetic inhibition by H_2O [39,40]. This suggests that when CO_2 conversion is lower than RWGS equilibrium conversion, the RWGS reaction is dominant and there is a lack of driving force for the FTS. At higher CO_2 conversions, the rate of CO_2 conversion are determined by FTS reaction.

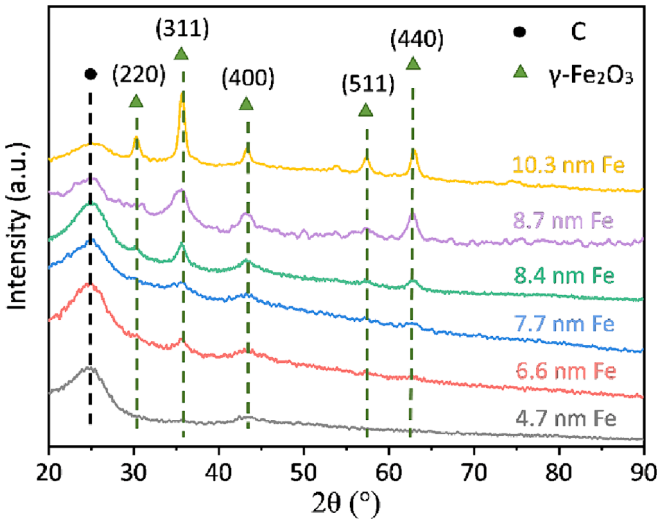

Fig. 1. The XRD pattern of carbon-supported Fe catalysts.

In order to understand the reaction pathway of CO_2-FTS, the relation between CO selectivity and CO_2 conversion was investigated. A recent review by Krausser et al. pointed out that limited data is available in literature on selectivity-conversion relationships although they are useful for the identification of individual reaction pathways [41]. As shown in Fig. 3(b), the CO selectivity decreased with increasing CO_2 conversion. At low CO_2 conversion, i.e. less than 10 %, the CO selectivity was almost 100 % in all cases, suggesting that CO is directly formed from CO_2 via RWGS as the primary reaction. This also implied that the Sabatier reaction (the catalytic reduction of CO_2 towards methane) played an insignificant role in carbon-supported Fe-based CO_2-FTS catalyst systems, which is contrary to the zirconia-supported Fe-based CO_2-FTS catalyst systems [36]. CO was further converted into hydrocarbons via FTS as the secondary reaction. In contrast to literature which reported a linear relationship between CO_2 conversion and CO selectivity, we found an inverse S-shaped relationship which coincided with the thermodynamic constraints [36,42,43]. Two trends of CO selectivity based on average Fe particle size were observed, namely 4.7 to 7.7 nm Fe (dotted line) and 8.4 to 10.3 nm Fe (solid line). Therefore, the CO selectivity is associated with CO_2 conversion and Fe particle size. As the CO_2-FTS reaction is consecutive, the effects of particle size on product selectivity of the RWGS and FTS reactions are discussed separately.

3.3. Effect of particle size on RWGS and FTS reactions

To investigate the particle size effects on the RWGS reaction, two catalysts with an identical Fe loading of 5 wt% but different average Fe

Table 1
Properties of fresh carbon-supported Fe catalysts.

Catalyst	Weight % loading [a]		Average Particle Size of Fe_2O_3 (nm) [b]	Fe_2O_3 crystallite size (nm) [c]	S_{BET} (m^2g^{-1}) [d]	V_{SPD} (cm^3g^{-1}) [d]	D_{BJH} (nm) [d]
	Fe	K					
carbon black	–	–	–	–	243	0.7	15
4.7 nm Fe	2.2	0.1	4.7 ± 1.0	–	171	0.5	17
6.6 nm Fe	4.6	0.2	6.6 ± 1.6	–	196	0.5	15
7.7 nm Fe	8.5	0.5	7.7 ± 1.6	4.0	167	0.5	15
8.4 nm Fe*	4.6	0.2	8.4 ± 1.8	5.2	171	0.6	16
8.7 nm Fe	18.7	1.2	8.7 ± 1.8	5.4	111	0.4	16
10.3 nm Fe**	18.7	1.2	10.3 ± 2.3	7.6	123	0.5	16

[a] Measured with ICP-OES;
[b] Number average determined by TEM;
[c] Calculated by XRD;
[d] Measured with N_2-adsorption, S_{BET}: Specific surface, V_{SPD}: Pore volume, D_{BJH}: Pore size; *: pyrolyzed at 700 °C for 8 h; **: pyrolyzed at 500 °C for 32 h.

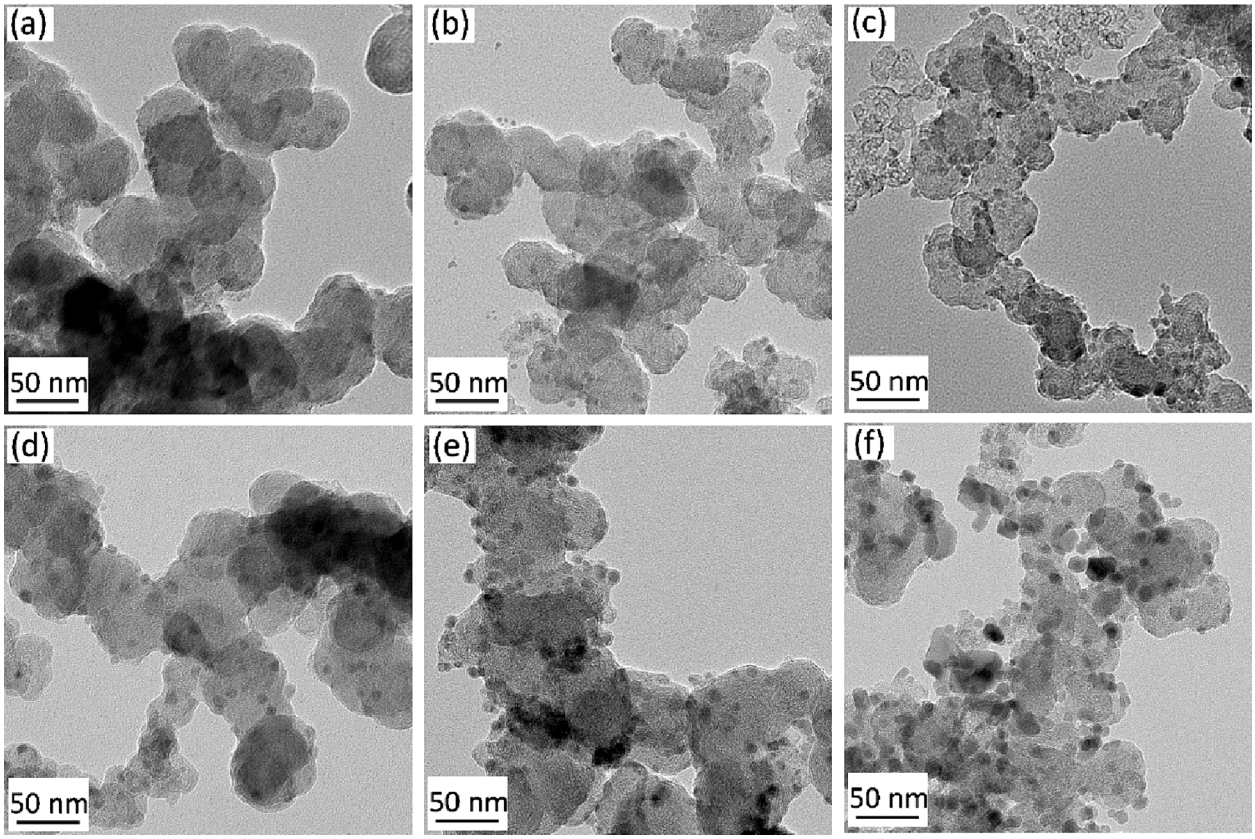

Fig. 2. TEM images of fresh catalysts: (a) 4.7 nm Fe, (b) 6.6 nm Fe, (c) 7.7 nm Fe, (d) 8.4 nm Fe, (e) 8.7 nm Fe, and (f) 10.3 nm Fe.

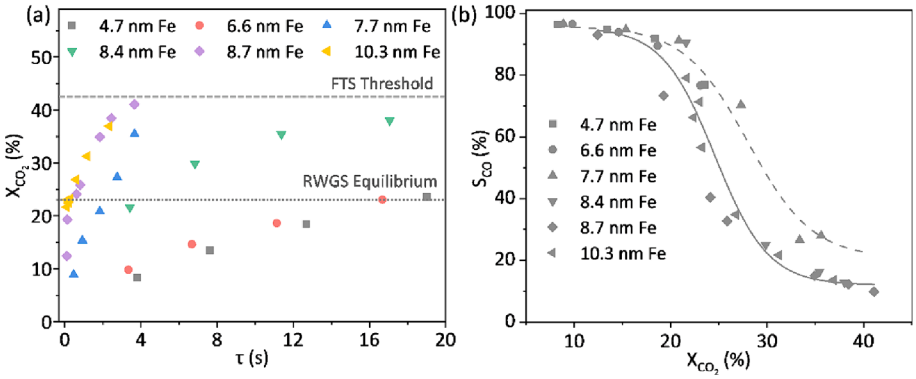

Fig. 3. (a) CO_2 conversion versus residence time; (b) CO selectivity versus CO_2 conversion (300 °C, 11 bar, $H_2/CO_2 = 3$, 600-72000 $mL \cdot g_{cat}^{-1} \cdot h^{-1}$), dotted line: fitting based on 4.7 to 7.7 nm Fe, solid line: fitting based on 8.4 to 10.3 nm Fe.

particle size (6.6 and 8.4 nm) were studied. As shown in Fig. 4 (a), the 8.4 Fe nm catalyst showed a higher CO_2 conversion at the same residence time, indicating a higher intrinsic activity of the larger Fe nanoparticles. In addition, the higher CO_2 conversion resulted in lower CO selectivity (Fig. 4(b)). Both observations were also reported by Zhu et al. for zirconia-supported Fe-based catalysts, and they further found different particle size effects on RWGS at 7 and 13 % CO_2 conversion. At 7 % CO_2 conversion, the CO selectivity was consistent at 80 % between the particle size of 2.5 to 6.1 nm whereas at 13 % CO_2 conversion, CO selectivity decreased over the entire range of 2.5 nm to 12.9 nm [36]. In our study, the CO selectivity was 90 % for both the 6.6 and 8.4 nm Fe catalysts at 20 % CO_2 conversion. It appears that the differences in CO selectivity at identical conditions were a result of CO_2 conversion instead of the particle size. Hence, the particle size effect was more significant for activity than selectivity.

To decouple the impact of CO_2 conversion and Fe particle size on hydrocarbon selectivity, the hydrocarbon selectivity was plotted as a function of CO_2 conversion. From Fig. 4(c), the CH_4 selectivity increased with increasing CO_2 conversion, suggesting that CH_4 is predominantly formed through CO and there is insignificant Sabatier activity. No clear influence of particle size on CH_4 selectivity was observed. Similar positive trends for C_2-C_4 and C_{5+} selectivity with CO_2 conversion were shown in Fig. 4(d) and (e) respectively. On the other hand, clear relations were found between particle size and the ratio of olefin and paraffin (O/P) for C_2-C_4 hydrocarbons, as presented in Fig. 4(f). Compared to the 8.4 nm Fe catalyst, the 6.6 nm Fe catalyst shows a lower ratio of O/P, indicating that it produced more C_2-C_4 paraffins and less C_2-C_4 olefins. Smaller particles were proposed to favor H_2 adsorption and dissociation, leading to higher H surface coverages and lower O/P ratios [35]. Regardless of particle size, the ratio of O/P decreased

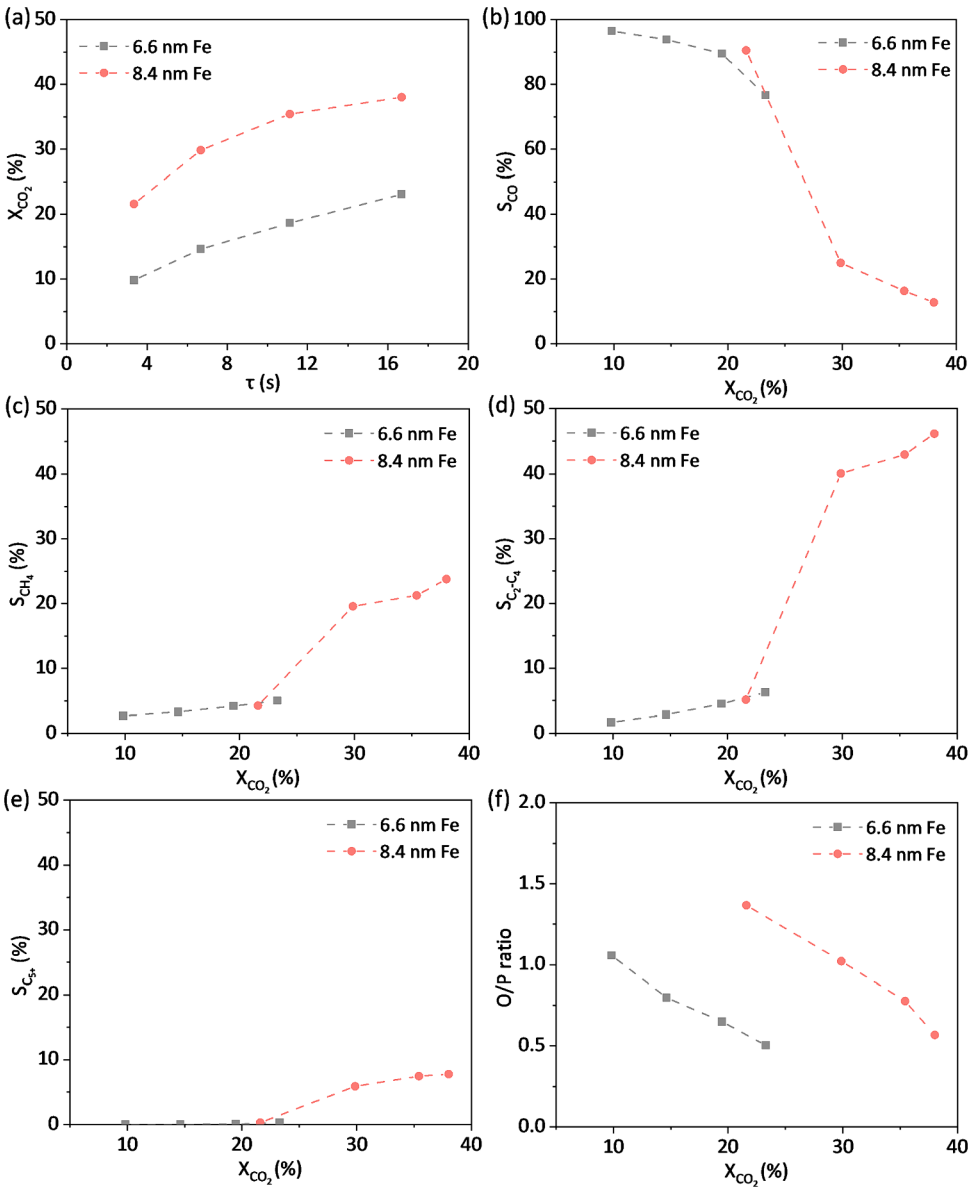

Fig. 4. (a) CO_2 conversion versus residence time; (b) CO selectivity versus CO_2 conversion; (c-e) HC selectivity versus CO_2 conversion and (f) O/P ratio for C_2-C_4 hydrocarbons over 6.6 and 8.4 nm Fe catalysts (300 °C, 11 bar, $H_2/CO_2 = 3$, 600-3000 mL·g_{cat}^{-1}·h^{-1}).

with increasing CO_2 conversion, and this is consistent with a higher degree of secondary FTS reactions such as olefin hydrogenation and/or oligomerization occurring at higher CO conversions [44].

The catalytic stability of both catalysts was evaluated at 300 °C, 11 bar, $H_2/CO_2 = 3$, $X_{CO2} \approx 20$ % over 20 h time-on-stream (Fig. S3). CO_2 conversion, CO- and hydrocarbon selectivity remained stable during this period, except for an initial activation period of approximately 4 h.

3.4. Catalytic performance at similar CO_2 conversions

To exclude the effect of CO_2 conversion, it is critical to evaluate selectivity at similar CO_2 conversion levels. Fig. 5(a) and (b) show product selectivity at $X_{CO2} \approx 20$ % and $X_{CO2} \approx 35$ % respectively. The corresponding hydrocarbon distribution and chain growth probability are included in the Supporting Information as Figs. S4 and S5. A summary of catalyst performance of bulk and supported Fe-based catalysts is included as Table S1 in the Supporting Information. At 20 % CO_2 conversion, the four catalysts with smallest iron particle sizes (4.7 to 8.4 nm) exhibited similar (around 90 %) CO selectivity, suggesting that the

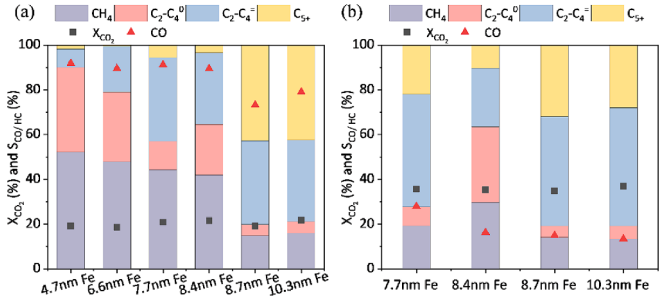

Fig. 5. Catalytic performance for CO_2-FTS at (a) $X_{CO2} \approx 20$ %; (b) $X_{CO2} \approx 35$ % over the catalysts with various particle size (300 °C, 11 bar, $H_2/CO_2 = 3$, 600-72000 mL·g_{cat}^{-1}·h^{-1}).

primary reaction was not structure sensitive within this particle size range. The 8.7 and 10.3 nm Fe catalysts (both 20 wt% Fe loading) showed lower CO selectivity and higher selectivity towards C_{2+}

products. As the decrease in CO selectivity did not correspond to a higher methane selectivity, the dominant primary reaction remained to be RWGS and no structure sensitivity influence was observed for the primary reaction within this particle size range. This is in contrast to the particle size effect study by Zhu et al., in which the larger Fe nanoparticles supported on zirconia catalyzed both RWGS and methanation primary reactions [36]. For the secondary FTS reaction, the CH_4 and C_2-C_4 paraffin selectivity decreased while C_2-C_4 olefins and C_{5+} selectivity increased very significantly with the increasing particle size. The methane selectivity dropped from 52 to 15 % when the iron particle size increased from 4.7 to 10.3 nm amid an increase in C_{5+} selectivity from 2 to 43 %. The higher selectivity towards paraffinic products of the smaller Fe nanoparticles has been earlier reported in CO-FTS literature [45–47]. Galvis et al. proposed the higher production of methane from small iron carbide nanoparticles to be due to the abundance of corners and edges, which are low coordination sites [46]. Iablokov et al. observed a similar trend and attributed the enhancement of methane formation to the edges and kinks sites which favor CO dissociation [47]. Besides, it has been put forward that the stronger H_2 adsorption and dissociation over smaller particles increase the ratio of H over CH_x surface coverage, hindering the C-C coupling and resulting in more light hydrocarbons production and lower ratio of olefin and paraffin [35,48]. Xie et al. verified that smaller Fe nanoparticles possessed higher H coverages, which displayed a positive correlation with CH_4 selectivity [22].

At 35 % CO_2 conversion, the CO selectivity decreased for catalysts with Fe nanoparticles in the range of 7.7 to 10.3 nm, implying that larger particles are more active for the secondary FTS reaction. As the catalysts with smaller Fe nanoparticles possessed lower activity, 35 % CO_2 conversion could not be reached with the current reactor set-up configuration, i.e. mass flow controllers and reactor size. Regarding the hydrocarbon distribution, CH_4 and C_2-C_4 paraffins selectivity decreased, C_2-C_4 olefins selectivity remained constant, and C_{5+} selectivity increased with the increasing particle size, except for 8.4 nm Fe catalyst. The difference of 8.4 nm Fe catalyst in hydrocarbon selectivity may be due to the lower K loading. The K loading can affect the olefin/paraffin ratio by influencing the H_2 dissociation and adsorption [49]. In summary, at both CO_2 conversion levels, a low CO selectivity was obtained over large particles with a more active secondary FTS reaction. Small Fe nanoparticles exhibit a propensity to produce CH_4 and C_2-C_4 paraffins, while larger Fe nanoparticles tend to produce long-chain hydrocarbons.

3.5. Fe particle size growth

Fig. 6 shows the TEM images and Fe particle size distributions of activated and spent catalysts (6.6 and 8.7 nm Fe). After the activation protocol consisting of reduction and carburization, the Fe nanoparticle size of the 6.6 nm and 8.7 nm Fe catalysts grew with 1.4 and 1.3 nm respectively. After 20 h time-on-stream, the average sizes of the 6.6 nm and 8.7 nm Fe spent catalysts had further grown to 9.2 and 13.5 nm respectively. The particle size distributions are provided in Fig. 6(c) and (f) respectively. The distribution for both catalysts increased even more than the average particle size. The largest increase in particle size and particle size distribution is observed with the 20 wt% loaded catalyst (8.7 nm) showing particles with sizes of around 25 nm.

3.6. In situ Mössbauer spectroscopy

To identify the various Fe phases during reduction, carburization and CO_2-FTS reaction, in situ Mössbauer spectroscopy experiments were conducted for the 6.6 nm and 8.7 nm catalysts. These experiments were considered as in situ, because the catalysts were treated under identical reaction conditions (feed, temperature and pressure) as in performance evaluation experiments, and measured without exposure to air [50–52]. The spectra were collected at 120 K, as Mössbauer spectroscopy is optimally performed at cryogenic temperatures. The recoil-free gamma ray resonance (Mössbauer effect) is drastically reduced at high temperatures (when atoms are vibrating more). At low temperatures, the differences in the measured signals due to variations in the Debye temperatures (measure of the Fe bonding strengths) of the different Fe species are reduced. At high temperatures, the Fe structures become

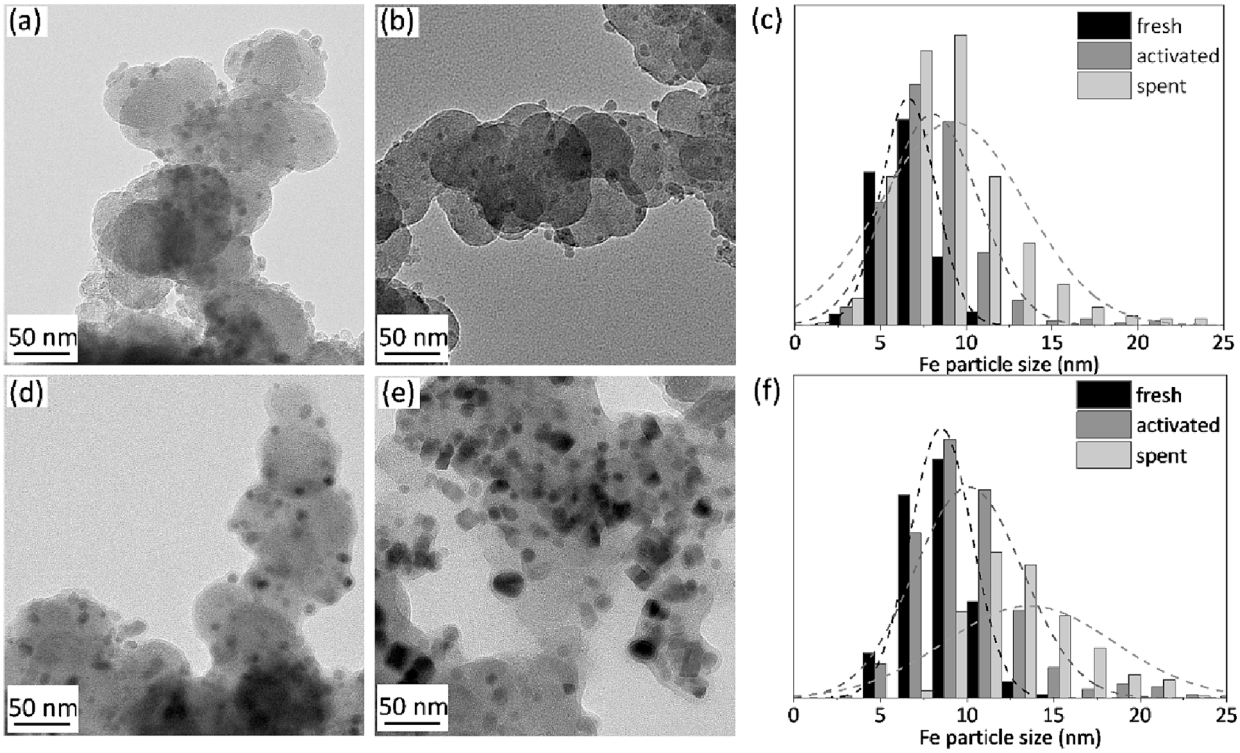

Fig. 6. TEM images of (a) activated 6.6 nm Fe, (b) spent 6.6 nm Fe, (d) activated 8.7 nm Fe, and (e) spent 8.7 nm Fe; and Fe particle size distribution of (c) 6.6 nm Fe and (f) 8.7 nm Fe (300 °C, 11 bar, $H_2/CO_2 = 3$, 1500 $mL \cdot g_{cat}^{-1} \cdot h^{-1}$, TOS = 20 h).

paramagnetic (especially those with nanometer size), preventing the accurate identification of the Fe species (by means of their magnetic field).

The spectra and Fe phase distributions are shown in Fig. 7. Further details on the Mössbauer fitted parameters can be found in Table S2 and S3. Both fresh catalysts contained 100 % Fe_2O_3, which is consistent with the XRD results. After reduction, both samples contained 20 % metallic Fe and 80 % FeO, indicating that the particle size had insignificant influence on the reduction step. After carburization, the 6.6 nm Fe catalyst contained 21 % ε'-$Fe_{2.2}C$ and 79 % FeO, indicating that metallic Fe was easier to be carburized to ε'-$Fe_{2.2}C$ as compared to FeO. A notable difference is the presence of 15 % of χ-Fe_5C_2 after carburization of the 8.7 nm Fe catalyst in comparison to the 6.6 nm catalyst. Under reaction conditions, the Fe phase composition of the 6.6 nm Fe catalyst did not change. On the other hand, the 8.7 nm Fe catalyst became almost fully carburized, consisting of 94 % χ-Fe_5C_2 and 6 % Fe_3O_4. The higher extent

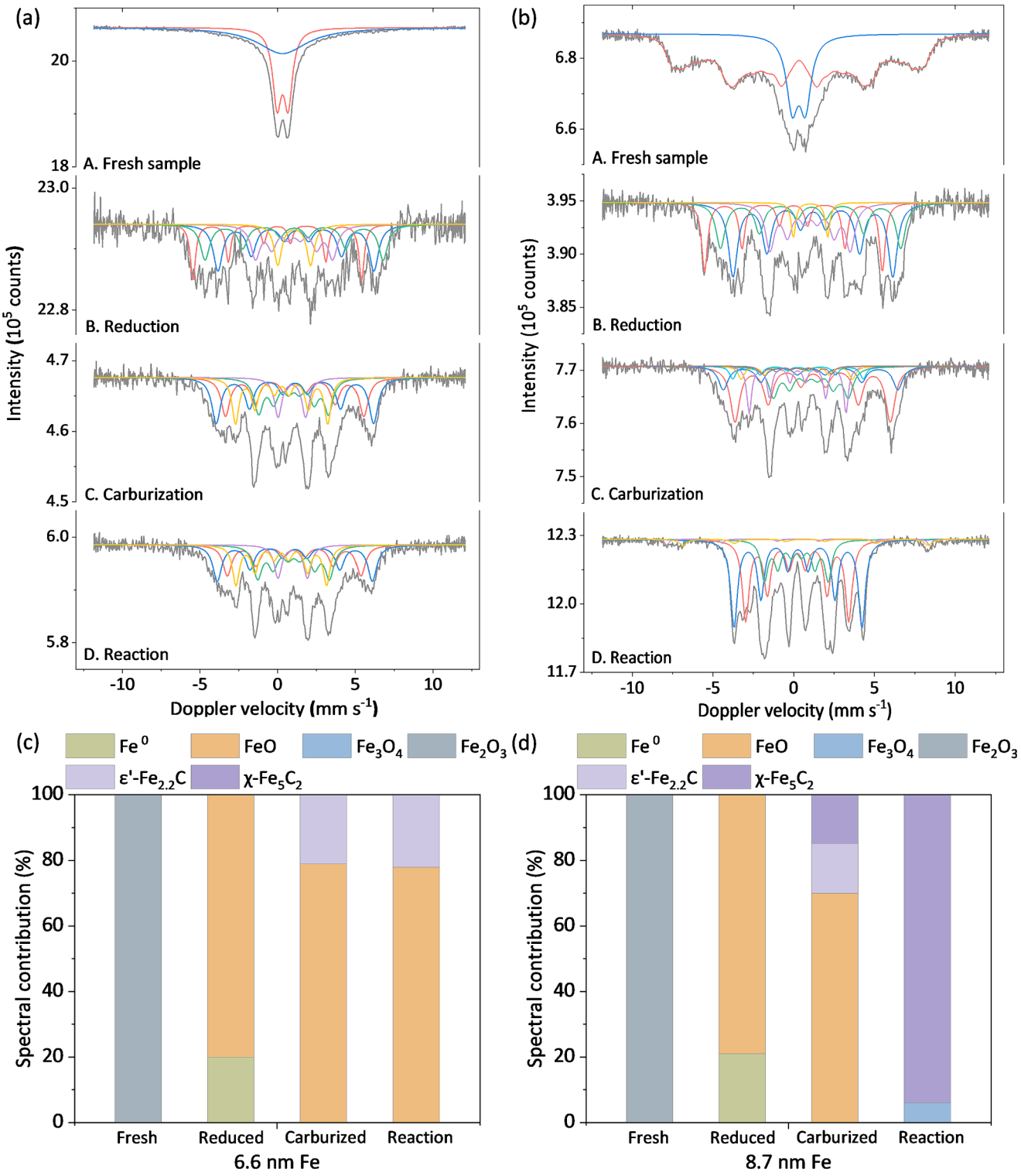

Fig. 7. Mössbauer spectra obtained in-situ with the (a) 6.6 nm Fe and (b) 8.7 nm Fe catalysts at 120 K; the Fe phases distribution in fresh, reduced, carburized, and reaction samples of 6.6 nm Fe (c) and 8.7 nm Fe (d) catalysts.

of carburization in larger particles was also reported previously by Kang et al for Fe_2O_3 nanocrystallites up to 16 nm [53]. However, according to Liu et al, there appears to be an inverse relation between carburization and particle size for Fe_3O_4 between 85 and 400 nm [54]. χ-Fe_5C_2 and Fe_3O_4 were reported to be the active phase for FTS and RWGS respectively and this can be used to explain the catalytic differences seen in Fig. 5. High selectivity towards CO and low selectivity towards long hydrocarbons was observed with the 6.6 nm Fe sample, which mostly consisted of FeO. On the other low selectivity towards CO and high selectivity towards Fischer-Tropsch products is seen with the sample consisting of Hägg carbide. Hence, the Fe phases from in situ Mössbauer during CO_2-FTS were in line with the catalytic performances over various particle size catalysts.

4. Conclusion

In this study, carbon-supported iron-based catalysts were used to gain a deeper understanding of the interplay between RWGS and FTS in the CO_2-FTS process. By varying the Fe loading from 2 to 20 wt%, as well as changing temperature and duration of calcination, catalysts containing Fe_2O_3 nanoparticles with average particle size of 4 to 10 nm were obtained. N_2 physisorption, ICP-OES, XRD, and TEM were used to identify the chemical and physical properties of the catalysts. At 300 °C, 11 bar, $H_2/CO_2 = 3$, the RWGS equilibrium conversion is 23 % and CO consumption via FTS enables a shift to 42 %. Our results confirm that CO_2-FTS consists of RWGS as the primary reaction and FTS as the secondary reaction. The Sabatier reaction is negligible over the carbon-supported Fe-based catalysts. Comparing two catalysts with identical 5 wt% Fe loading but different average Fe nanoparticle size (6.6 and 8.4 nm), the 8.4 nm Fe catalyst was at least two times more active than the 6.6 nm Fe catalyst. The CO selectivity and hydrocarbon chain growth probability were mainly influenced by CO_2 conversion while the olefin/paraffin ratio was dependent on Fe nanoparticle size. At similar CO_2 conversion of 20 or 35 %, lower CO selectivity and higher C_{2+} hydrocarbon product yield were observed over the larger Fe nanoparticles, while smaller Fe nanoparticles exhibited a propensity to produce paraffins due to lower coordination sites. In situ Mössbauer spectroscopy showed that the lower carburization level of the catalyst with smaller iron particle size limited the consecutive FTS reaction and resulted in high CO selectivity. Similarly complete carburization of the catalyst with larger particle size was seen which linked to the high selectivity towards long chain hydrocarbon products and low CO selectivity. We found that particle size could be used to tune the iron phase composition, resulting in improved performance. However, we are not able to decouple the influences of particle size from iron species and future work could be in this direction.

From our study, we demonstrated that selectivity control to CO or higher hydrocarbons is complex and dependent on numerous factors. The first factor is thermodynamics. At CO_2 conversion below the RWGS equilibrium conversion, RWGS dominates. To achieve higher selectivity towards C_{2+} hydrocarbons, CO_2 conversion needs to be higher than the RWGS equilibrium. The second factor is CO_2 conversion, and higher CO_2 conversion leads to higher hydrocarbon selectivity. The third factor is Fe nanoparticle size, and larger Fe nanoparticles were easier to carburize, leading to higher CO_2 conversion and hydrocarbon selectivity.

CRediT authorship contribution statement

Weixin Meng: Writing – review & editing, Writing – original draft, Validation, Methodology, Investigation, Formal analysis, Data curation, Conceptualization. **Bart C.A. de Jong:** Writing – review & editing, Validation, Methodology, Investigation, Formal analysis, Data curation. **Henk van de Bovenkamp:** Writing – review & editing, Methodology. **Gert-Jan Boer:** Writing – review & editing, Methodology. **G. Leendert Bezemer:** Writing – review & editing, Methodology, Conceptualization. **A. Iulian Dugulan:** Writing – review & editing, Validation, Resources, Methodology, Investigation, Formal analysis, Data curation, Conceptualization. **Jingxiu Xie:** Writing – review & editing, Writing – original draft, Supervision, Resources, Project administration, Methodology, Funding acquisition, Formal analysis, Conceptualization.

Declaration of competing interest

The authors declare that they have no known competing financial interests or personal relationships that could have appeared to influence the work reported in this paper.

Data availability

Data will be made available on request.

Acknowledgements

Weixin Meng acknowledges financial support from the China Scholarship Council (CSC): NO. 202106460008.

Appendix A. Supplementary data

Supplementary data to this article can be found online at https://doi.org/10.1016/j.cej.2024.151166.

References

[1] C. Hepburn, E. Adlen, J. Beddington, E.A. Carter, S. Fuss, N. Mac Dowell, J.C. Minx, P. Smith, C.K. Williams, The technological and economic prospects for CO_2 utilization and removal, Nature 575 (2019) 87–97, https://doi.org/10.1038/s41586-019-1681-6.

[2] A.D.N. Kamkeng, M. Wang, J. Hu, W. Du, F. Qian, Transformation technologies for CO_2 utilisation: Current status, challenges and future prospects, Chem. Eng. J. 409 (2021) 128138, https://doi.org/10.1016/j.cej.2020.128138.

[3] A. Saravanan, P. Senthil kumar Dai-Viet, N. Vo, S. Jeevanantham, V. Bhuvaneswari, V. Anantha Narayanan, P.R. Yaashikaa, S. Swetha, B. Reshma, A comprehensive review on different approaches for CO_2 utilization and conversion pathways, Chem. Eng. Sci. 236 (2021) 116515, https://doi.org/10.1016/j.ces.2021.116515.

[4] W. Zhou, K. Cheng, J. Kang, C. Zhou, V. Subramanian, Q. Zhang, Y. Wang, New horizon in C1 chemistry: breaking the selectivity limitation in transformation of syngas and hydrogenation of CO_2 into hydrocarbon chemicals and fuels, Chem. Soc. Rev. 48 (2019) 3193–3228, https://doi.org/10.1039/C8CS00502H.

[5] D. Wang, Z. Xie, M.D. Porosoff, J.G. Chen, Recent advances in carbon dioxide hydrogenation to produce olefins and aromatics, Chem 7 (2021) 2277–2311, https://doi.org/10.1016/j.chempr.2021.02.024.

[6] T. Riedel, G. Schaub, K.W. Jun, K.W. Lee, Kinetics of CO_2 Hydrogenation on a K-Promoted Fe Catalyst, Ind. Eng. Chem. Res. 40 (2001) 1355–1363, https://doi.org/10.1021/ie000084k.

[7] R.M. Bown, M. Joyce, Q. Zhang, T.R. Reina, M.S. Duyar, Identifying commercial opportunities for the reverse water gas shift reaction, Energy Technol. 9 (2021) 210054, https://doi.org/10.1002/ente.202100554.

[8] L. Yang, L. Pastor-Pérez, J.J. Villora-Pico, S. Gua, A. Sepúlveda-Escribano, T. R. Reina, CO_2 valorisation via reverse water-gas shift reaction using promoted Fe/CeO_2-Al_2O_3 catalysts: Showcasing the potential of advanced catalysts to explore new processes design, Appl. Catal. A 593 (2020) 117442, https://doi.org/10.1016/j.apcata.2020.117442.

[9] A.Y. Khodakov, W. Chu, P. Fongarland, Advances in the development of novel cobalt Fischer-Tropsch catalysts for synthesis of long-chain hydrocarbons and clean fuels, Chem. Rev. 107 (2007) 1692–1744, https://doi.org/10.1021/cr050972v.

[10] G.P. Van Der Laan, A. Beenackers, Kinetics and selectivity of the Fischer-Tropsch Synthesis: A literature review, Catal. Rev. 41 (1999) 255–318, https://doi.org/10.1081/CR-100101170.

[11] O.O. James, B. Chowdhury, M.A. Mesubi, S. Maity, Reflections on the chemistry of the Fischer-Tropsch synthesis, RSC Adv. 2 (2012) 7347–7366, https://doi.org/10.1039/C2RA20519J.

[12] S. Lyu, L. Wang, Z. Li, S. Yin, J. Chen, Y. Zhang, J. Li, Y. Wang, Stabilization of ε-iron carbide as high-temperature catalyst under realistic Fischer-Tropsch synthesis conditions, Nat. Commun. 11 (2020) 6219, https://doi.org/10.1038/s41467-020-20068-5.

[13] P. Wang, W. Chen, F.K. Chiang, A.I. Dugulan, Y. Song, R. Pestman, K. Zhang, J. Yao, B. Feng, P. Miao, W. Xu, E.J.M. Hensen, Synthesis of stable and low-CO_2 selective ε-iron carbide Fischer-Tropsch catalysts, Sci. Adv. 4 (2018) eaau2947, https://doi.org/10.1126/sciadv.aau2947.

[14] E. de Smit, B.M. Weckhuysen, The renaissance of iron-based Fischer-Tropsch synthesis: on the multifaceted catalyst deactivation behaviour, Chem. Soc. Rev. 37 (2008) 2758–2781, https://doi.org/10.1039/B805427D.

[15] J. Xie, H.M.T. Galvis, A.C.J. Koeken, A. Kirilin, A.I. Dugulan, M. Ruitenbeek, K. P. de Jong, Size and promoter effects on stability of carbon-nanofiber-supported iron-based Fischer-Tropsch catalysts, ACS Catal. 6 (2016) 4017–4024, https://doi.org/10.1021/acscatal.6b00321.

[16] H.M.T. Galvis, K.P. de Jong, Catalysts for production of lower olefins from synthesis gas: A review, ACS Catal. 3 (2013) 2130–2149, https://doi.org/10.1021/cs4003436.

[17] Q. Zhang, W. Deng, Y. Wang, Recent advances in understanding the key catalyst factors for Fischer-Tropsch synthesis, J. Energy Chem. 22 (2013) 27–38, https://doi.org/10.1016/S2095-4956(13)60003-0.

[18] C. Qin, Y. Du, K. Wu, Y. Xu, R. Li, H. Fan, D. Xu, M. Ding, Facet-Controlled Cu-doped and K-promoted Fe_2O_3 nanosheets for efficient CO_2 hydrogenation to liquid hydrocarbons, Chem. Eng. J. 467 (2023) 143403, https://doi.org/10.1016/j.cej.2023.143403.

[19] W. Li, H. Wang, X. Jiang, J. Zhu, Z. Liu, X. Guo, C. Song, A short review of recent advances in CO_2 hydrogenation to hydrocarbons over heterogeneous catalysts, RSC Adv. 8 (2018) 7651–7669, https://doi.org/10.1039/C7RA13546G.

[20] Q. Zhang, J. Kang, Y. Wang, Development of novel catalysts for Fischer-Tropsch Synthesis: Tuning the product selectivity, ChemCatChem 2 (2010) 1030–1058, https://doi.org/10.1002/cctc.201000071.

[21] H. Zhao, L. Guo, W. Gao, F. Chen, X. Wu, K. Wang, Y. He, P. Zhang, G. Yang, N. Tsubaki, Multi-promoters regulated iron catalyst with well-matching reverse water-gas shift and chain propagation for boosting CO_2 hydrogenation, J. CO_2 Util. 52 (2021) 101700, https://doi.org/10.1016/j.jcou.2021.101700.

[22] J. Xie, J. Yang, A.I. Dugulan, A. Holmen, D. Chen, K.P. de Jong, M.J. Louwerse, Size and promoter effects in supported iron Fischer-Tropsch catalysts: Insights from experiment and theory, ACS Catal. 6 (2016) 3147–3157, https://doi.org/10.1021/acscatal.6b00131.

[23] H.M. Torres Galvis, J.H. Bitter, C.B. Khare, M. Ruitenbeek, A.I. Dugulan, K.P. de Jong, Supported iron nanoparticles as catalysts for sustainable production of lower olefins, Science 335 (2012) 835–838, https://doi.org/10.1126/science.1215614.

[24] C.C. Amoo, J.I. Orege, Q. Ge, J. Sun, Exploiting the latency of carbon as catalyst in CO_2 hydrogenation, Chem. Eng. J. 471 (2023) 144606, https://doi.org/10.1016/j.cej.2023.144606.

[25] A.J. Barrios, D.V. Peron, A. Chakkingal, A.I. Dugulan, S. Moldovan, K. Nakouri, J. Thuriot-Roukos, R. Wojcieszak, J.W. Thybaut, M. Virginie, A.Y. Khodakov, Efficient promoters and reaction paths in the CO_2 hydrogenation to light olefins over zirconia-supported iron catalysts, ACS Catal. 12 (2022) 3211–3225, https://doi.org/10.1021/acscatal.1c05648.

[26] A.J. Barrios, B. Gu, Y. Luo, D.V. Peron, P.A. Chernavskii, M. Virginie, R. Wojcieszak, J.W. Thybaut, V.V. Ordomsky, A.Y. Kov, Identification of efficient promoters and selectivity trends in high temperature Fischer-Tropsch synthesis over supported iron catalysts, Appl. Catal. b: Environ. 273 (2020) 119028, https://doi.org/10.1016/j.apcatb.2020.119028.

[27] B. Liang, T. Sun, J. Ma, H. Duan, L. Li, X. Yang, Y. Zhang, X. Su, Y. Huang, T. Zhang, Mn decorated Na/Fe catalysts for CO_2 hydrogenation to light olefins, Catal, Sci. Technol. 9 (2019) 456–464, https://doi.org/10.1039/C8CY02275E.

[28] N. Chaipraditgul, T. Numpilai, C. Kui Cheng, N. Siri-Nguan, T. Sornchamni, C. Wattanakit, J. Limtrakul, T. Witoon, Tuning interaction of surface-adsorbed species over Fe/K-Al_2O_3 modified with transition metals (Cu, Mn, V, Zn or Co) on light olefins production from CO_2 hydrogenation, Fuel 283 (2021) 119248, https://doi.org/10.1016/j.fuel.2020.119248.

[29] Y. Han, C. Fang, X. Ji, J. Wei, Q. Ge, J. Sun, Interfacing with carbonaceous potassium promoters boosts catalytic CO_2 hydrogenation of iron, ACS Catal. 10 (2020) 12098–12108, https://doi.org/10.1021/acscatal.0c03215.

[30] L. Xiong, S. Liu, Y. Men, L. Li, X. Niu, K. Guo, J. Xu, W. An, J. Wang, Y. Cong, Highly selective hydrogenation of CO_2 to C_{5+} hydrocarbons over Fe catalysts copromoted by K with Pd, J. Environ. Chem. Eng. 10 (2022) 108407, https://doi.org/10.1016/j.jece.2022.108407.

[31] Q. Yan, A.S.A. Matvienko, H. Lun, M. Holena, E.V. Kondratenko, Revealing property-performance relationships for efficient CO_2 hydrogenation to higher hydrocarbons over Fe-based catalysts: Statistical analysis of literature data and its experimental validation, Appl. Catal. B-Environ. 282 (2021) 119554, https://doi.org/10.1016/j.apcatb.2020.119554.

[32] L. Barberis, A.H. Hakimioun, P.N. Plessow, N.L. Visser, J.A. Stewart, B. D. Vandegehuchte, F. Studt, P.E. de Jongh, Competition between reverse water gas shift reaction and methanol synthesis from CO_2: influence of copper particle size, Nanoscale 14 (2022) 13551, https://doi.org/10.1039/D2NR02612K.

[33] H. Wu, Y. Chang, J. Wu, J. Lin, I. Linc, C. Chen, Methanation of CO_2 and reverse water gas shift reactions on Ni/SiO_2 catalysts: the influence of particle size on selectivity and reaction pathway, Catal, Sci. Technol. 5 (2015) 4154–4163, https://doi.org/10.1039/C5CY00667H.

[34] J. Liu, P. Wang, W. Xu, E.J.M. Hensen, Particle size and crystal phase effects in Fischer-Tropsch catalysts, Eng. 3 (2017) 467–476, https://doi.org/10.1016/J.ENG.2017.04.012.

[35] X. Han, J. Lv, S. Huang, Q. Zhao, Y. Wang, Z. Li, X. Ma, Size dependence of carbon-encapsulated iron-based nanocatalysts for Fischer-Trposch synthesis, Nano Res. 16 (5) (2023) 6270–6277, https://doi.org/10.1007/s12274-023-5417-4.

[36] J. Zhu, G. Zhang, W. Li, X. Zhang, F. Ding, C. Song, X. Guo, Deconvolution of the particle size effect on CO_2 hydrogenation over iron-based catalysts, ACS Catal. 10 (2020) 7424–7433, https://doi.org/10.1021/acscatal.0c01526.

[37] T. Xie, J. Wang, F. Ding, A. Zhang, W. Li, X. Guo, C. Song, CO_2 hydrogenation to hydrocarbons over alumina-supported iron catalyst: Effect of support pore size, J. CO2 Util. 19 (2017) 202–208, https://doi.org/10.1016/j.jcou.2017.03.022.

[38] Y. Wei, D. Luo, C. Zhang, J. Liu, Y. He, X. Wen, Y. Yang, Y. Li, Precursor controlled synthesis of graphene oxide supported iron catalysts for Fischer-Tropsch synthesis, Catal, Sci. Technol. 8 (2018) 2883–2893, https://doi.org/10.1039/C8CY00617B.

[39] T. Hos, M.V. Landau, M. Herskowitz, Hydrogenation of CO_2 on Fe-based catalysts: Preferred route to renewable liquid fuels, Ind. Eng. Chem. Res. 61 (29) (2022) 10387–10399, https://doi.org/10.1021/acs.iecr.1c04254.

[40] L. Brübach, D. Hodonj, P. Pfeifer, Kinetic analysis of CO_2 hydrogenation to long-Chain hydrocarbons on a supported iron catalyst, Ind. Eng. Chem. Res. 61 (2022) 1644–1654, https://doi.org/10.1021/acs.iecr.1c04018.

[41] L. Krausser, Q. Yang, E.V. Kondratenko, CO_2 hydrogenation to hydrocarbons over Fe-based catalysts: Status and recent developments, ChemCatChem (2024) e202301716, https://doi.org/10.1002/cctc.202301716.

[42] Q. Yang, V.A. Kondratenko, S.A. Petrov, D.E. Doronkin, E. Saraçi, H. Lund, A. Arinchtein, R. Kraehnert, A.S. Skrypnik, A.A. Matvienko, E.V. Kondratenko, Identifying performance descriptors in CO_2 hydrogenation over iron-based catalysts promoted with alkali metals, Angew. Chem. Int. Ed. 61 (2022) e2021165, https://doi.org/10.1002/anie.202116517.

[43] A.S. Skrypnik, S.A. Petrov, V.A. Kondratenko, Q. Yang, H. Lund, A.A. Matvienko, E. V. Kondratenko, Descriptors affecting methane selectivity in CO_2 hydrogenation over unpromoted bulk iron(III)-based catalysts, ACS Catal. 12 (18) (2022) 11355–11368, https://doi.org/10.1021/acscatal.2c03375.

[44] J. Gorimbo, A. Muleja, X. Lu, Y. Yao, X. Liu, D. Hildebrandt, D. Glasser, Lu plot and Yao plot: Models to analyze product distribution of long-term gas-phase Fischer−Tropsch Synthesis experimental data on an iron catalyst, Energy Fuels 31 (5) (2017) 5682–5690, https://doi.org/10.1021/acs.energyfuels.7b00388.

[45] J.Y. Park, Y.J. Lee, P.K. Khanna, K.W. Jun, J.W. Bae, Y.H. Kim, Alumina-supported iron oxide nanoparticles as Fischer-Tropsch catalysts: Effect of particle size of iron oxide, J. Mol. Catal. Chem. 323 (2010) 84–90, https://doi.org/10.1016/j.molcata.2010.03.025.

[46] H.M.T. Galvis, J.H. Bitter, T. Davidian, M. Ruitenbeek, A.I. Dugulan, K.P. de Jong, Iron particle size effects for direct production of lower olefins from synthesis gas, J. Am. Chem. Soc. 134 (2012) 16207–16215, https://doi.org/10.1021/ja304958u.

[47] V. Iablokov, Y. Xiang, A. Meffre, P.F. Fazzini, B. Chaudret, N. Kruse, Size-dependent activity and selectivity of Fe/MCF-17 in the catalytic hydrogenation of carbon monoxide using Fe(0) nanoparticles as precursors, ACS Catal. 6 (2016) 2496–2500, https://doi.org/10.1021/acscatal.6b00346.

[48] A.N. Pour, M.R. Housaindokht, The olefin to paraffin ratio as a function of catalyst particle size in Fischer-Tropsch synthesis by iron catalyst, J. Nat. Gas Sci. Eng. 14 (2013) 204–210, https://doi.org/10.1016/j.jngse.2013.06.007.

[49] H. Chang, Q. Lin, M. Cheng, K. Zhang, B. Feng, J. Chai, Y. Lv, Z. Men, Effects of potassium loading over iron–silica interaction, phase evolution and catalytic behavior of precipitated iron-based catalysts for Fischer-Tropsch synthesis, Catal. 12 (2022) 916, https://doi.org/10.3390/catal12080916.

[50] Y. Zeng, X. Li, J. Wang, M.T. Sougrati, Y. Huang, T. Zhang, B. Liu, In situ/operando Mossbauer spectroscopy for probing heterogeneous catalysis, Chem Catal. 1 (2021) 1215–1233, https://doi.org/10.1016/j.checat.2021.08.013.

[51] T.A. Wezendonk, V.P. Santos, M.A. Nasalevich, Q.S.E. Warringa, A.I. Dugulan, A. Chojecki, A.C.J. Koeken, M. Ruitenbeek, G. Meima, H. Islam, G. Sankar, M. Makkee, F. Kapteijn, J. Gascon, Elucidating the nature of Fe species during pyrolysis of the Fe-BTC MOF into highly active and stable Fischer-Tropsch catalysts, ACS Catal. 6 (5) (2016) 3236–3247, https://doi.org/10.1021/acscatal.6b00426.

[52] Y. Zhou, A.S. Traore, D.V. Peron, A.J. Barrios, S.A. Chernyak, M. Corda, O. V. Safonova, A.I. Dugulan, O. Ersen, M. Virginie, V.V. Ordomsky, A.Y. Khodakov, Promotion effects of alkali metals on iron molybdate catalysts for CO_2 catalytic hydrogenation, J. Energy Chem. 85 (2023) 291–300, https://doi.org/10.1016/j.jechem.2023.06.019.

[53] K. Cheng, M. Virginie, V.V. Ordomsky, C. Cordier, P.A. Chernavskii, M.I. Ivantsov, S. Paul, Y. Wang, A.Y. Khodakov, Pore size effects in high-temperature Fischer-Tropsch synthesis over supported iron catalysts, J. Catal. 328 (2015) 139–150, https://doi.org/10.1016/j.jcat.2014.12.007.

[54] J. Liu, K. Li, Y. Song, C. Song, X. Guo, Selective hydrogenation of CO_2 to hydrocarbons: Effects of Fe_3O_4 particle size on reduction, carburization, and catalytic performance, Energy Fuel 35 (13) (2021) 10703–10709, https://doi.org/10.1021/acs.energyfuels.1c01265.